Negative specific heat in self-gravitating N-body systems enclosed in a spherical container with reflecting walls

Negative specific heat in self-gravitating *N*-body systems enclosed in a spherical container with reflecting walls

Nobuyoshi Komatsu,[1,*] Shigeo Kimura,[2] and Takahiro Kiwata[1]

[1]*Department of Mechanical Systems Engineering, Kanazawa University, Kakuma-machi, Kanazawa, Ishikawa 920-1192, Japan*
[2]*The Institute of Nature and Environmental Technology, Kanazawa University, Kakuma-machi, Kanazawa, Ishikawa 920-1192, Japan*

Gravity-dominated systems have a negative specific heat. We investigate the negative specific heat of self-gravitating systems enclosed in a spherical container with reflecting walls by means of *N*-body simulations. To simulate nonequilibrium processes, a particle reflected at a nonadiabatic wall is cooled to mimic energy loss by reflecting walls, while an adiabatic wall is employed for microcanonical ensembles. We show that a negative specific heat occurs not only in the microcanonical ensemble but also in certain nonequilibrium processes with the nonadiabatic wall. With increasing cooling rates, the dependence of temperature $\hat{T}$ on energy ε, i.e., the $\varepsilon - \hat{T}$ curve, gradually deviates from the microcanonical ensemble and approaches a certain common curve at a low-energy region. The common curve agrees with an $\varepsilon - \hat{T}$ curve for stellar polytropes, especially for the polytrope index of $n \sim 5$. We show that the stellar polytrope should be related to the present nonequilibrium process appearing in the self-gravitating system with the nonadiabatic wall. In the nonequilibrium process, a rapid change in velocity at the nonadiabatic wall significantly affects the velocity and density profiles. In particular, the greater the cooling rate, the greater the local velocity gradient at a low-energy region.

I. INTRODUCTION

Negative specific heat plays an important role in astrophysical phenomena such as in gravothermal catastrophe of globular clusters [1,2] and black hole thermodynamics [3,4]. Accordingly, the statistical mechanics and thermodynamics for long-range attractive interacting systems have been studied by many researchers [5–30]. For example, Lebowitz and Lieb [5] proved that a Coulomb system of electrons and nuclei always has a positive specific heat even in microcanonical ensembles, while Thirring [6] showed that a negative specific heat can only occur in an isolated system corresponding to microcanonical ensembles. Of course, there are exceptions to these results because of the assumptions used and, therefore, the thermodynamic properties of these systems have been examined [31–33]. In fact, a negative specific heat has been observed experimentally, e.g., in nuclear fragmentation [34] and atomic clusters [35].

In these works, Posch and Thirring [32] demonstrated a negative specific heat in a purely attractive interacting system enclosed in circular container walls. In their simulation, a particle reflected at the wall was cooled to mimic energy loss by radiation in stars and the dynamical evolution of the system was examined. That is, the container wall corresponds to a nonadiabatic wall for simulating a kind of nonequilibrium process. We expect, at least in principle, that such a nonadiabatic wall can control the thermodynamic properties of the system. However, it is not yet understood completely how a nonadiabatic wall affects the dynamical evolution of a system or the thermodynamic properties such as the incidence of negative specific heat for the best possible cooling agent [33]. Therefore, to acquire a deeper under-

standing of negative specific heat in a nonequilibrium process, it is necessary to investigate potential of the nonadiabatic wall or the influence of the nonadiabatic wall quantitatively. In this context, we examine a system enclosed in a spherical container with nonadiabatic walls by means of *N*-body simulations. In the present study, we focus on the influence of the nonadiabatic wall on the dynamical evolution of the system especially on the relationship between energy and temperature.

The present paper is organized as follows. In Sec. II, we give a brief review of numerical techniques for simulating a self-gravitating system enclosed in a spherical container with adiabatic and nonadiabatic walls. In Sec. III, we describe the initial conditions for the simulation. In Sec. IV, the simulation results are presented. In Sec. IV A, through a nonequilibrium process, we examine the influence of the nonadiabatic wall on the relationship between energy and temperature. Moreover, we investigate the nonequilibrium process by comparing with a quasiequilibrium structure of stellar polytropes. In Sec. IV B, we discuss the local properties of the system to observe the influence of the nonadiabatic wall. Finally, we present our conclusions.

II. *N*-BODY SIMULATION TECHNIQUES

We consider a system consisting of *N* point particles enclosed in a spherical container of radius *R*. To simulate a self-gravitating system, we integrate the set of classical equations of motion for the particles interacting through the Plummer softened potential,

$$\Phi = -\frac{1}{\sqrt{r^2 + r_0^2}}, \tag{1}$$

where r and r_0 represent the distance between particles and the softening parameter, respectively [36–38]. The total energy E of the system is defined as

$$E = E_{KE} + E_{PE} = \sum_i^N \frac{m_i v_i^2}{2} - \sum_{i<j}^N \frac{Gm_i m_j}{\sqrt{r_{ij}^2 + r_0^2}}, \qquad (2)$$

where E_{KE}, E_{PE}, and m_i represent kinetic energy, potential energy, and the mass of the ith point particle, respectively. G, v_i, and r_{ij} represent the gravitational constant, the speed of the ith particle, and the distance between the ith and jth particles, respectively. The mass of each particle is set to be m. To apply traditional conventions for self-gravitating systems, the total rescaled energy ε is defined as

$$\varepsilon = \varepsilon_{KE} + \varepsilon_{PE} = E\frac{R}{GM^2} = E\frac{R}{G(mN)^2}, \qquad (3)$$

where M, ε_{KE}, and ε_{PE} represent the total mass, rescaled kinetic and potential energies, respectively. All the energies are rescaled using Eq. (3). In this study, the units of time and velocity are $\sqrt{R^3/(Gm)}$ and $\sqrt{Gm/R}$, respectively [37]. The units are set to be $G=R=m=1$ to ensure generality of the system. In our units, the temperature $\hat{T}$ of the system is given by

$$\hat{T} = \frac{2}{3k_B}\varepsilon_{KE} = \frac{2}{3}\varepsilon_{KE}, \qquad (4)$$

assuming that the kinetic energy corresponds to the temperature and that Boltzmann's constant k_B is 1. That is, we focus on the temperature of the system and ignore the local distribution of temperature.

In this study, we consider a small system consisting of $N=250$ point particles in a spherical container of radius $R=1$. For simulating the N-body system, the set of equations of motion is integrated using Verlet's algorithm, i.e., the leapfrog algorithm,

$$\frac{\partial^2 x_i}{\partial t^2}(\Delta t)^2 = x_i(t+\Delta t) - 2x_i(t) + x_i(t-\Delta t) = \sum_j f_{ij}(t)(\Delta t)^2, \qquad (5)$$

where $f_{ij}(t)$ is a partial force from the jth particle on the ith particle located at position x_i at time t. To maintain the accuracy of our simulations, a time step Δt is selected as 10^{-5} based on a simulation with several different time steps [36,37]. Through the present simulations, all interparticle forces are calculated directly at each time step Δt. In this paper, all the results are averaged over 30 simulations with identically prepared initial setups to observe an averaged behavior of the system.

To mimic a spherical adiabatic wall for microcanonical ensembles, the radial component of the velocity of a particle is reversed when it reaches the wall [37]. Accordingly, the velocity speed $|\mathbf{v}_i|$ of the particle is conserved through the reflection. In contrast, to mimic a spherical nonadiabatic wall for nonequilibrium processes, the velocity after the reflection is reduced as

$$\mathbf{v}_i^{(reflected)} = (1 - \gamma)\mathbf{v}_i, \qquad (6)$$

where γ is a velocity reduction rate or a cooling rate [38]. (In this study, the nonadiabatic wall is employed to simulate energy loss by reflecting walls [39].) The cooling rate γ is

varied from 0.001 to 0.5 in order to investigate the influence of the nonadiabatic wall. Note that $\gamma=0$ corresponds to the adiabatic wall for a microcanonical ensemble. In the present method, all the components of the reflected velocity are reduced as described in Ref. [32]. That is, the nonadiabatic wall for a nonequilibrium process slightly influences total angular momentum of the present system [40]. In fact, it is known that total angular momentum affects a phase transition of rotating systems [41]. Therefore, we have checked the total angular momentum through our simulations and confirmed that a variation in total angular momentum is sufficiently small in the present study.

For the Plummer softened potential, the softening parameter r_0 is set to be $0.005R$. Accordingly, the collapse and explosion energies for the system with the adiabatic wall are $\varepsilon_{coll} \approx -0.339$ and $\varepsilon_{expl} \approx 0.267$, respectively [42]. This means, if the total rescaled energy ε of the uniform state becomes lower than ε_{coll}, the system should undergo a collapse to a core-halo state. In contrast, if the energy ε becomes higher than ε_{expl}, the system should undergo an explosion. When the energy of the system is between ε_{coll} and ε_{expl}, the system should be in a stable or metastable state. Note that the softening parameter r_0 affects the properties of the system. For example, for pure gravitational potentials, the collapse energy is -0.335, and a mean-field phase diagram or an $\varepsilon-\hat{T}$ curve has a spiral curve [7,10]. (For $r_0 = 0.005R$, the $\varepsilon-\hat{T}$ curve has high- and low-energy branches terminating at ε_{coll} and ε_{expl} [43].) Accordingly, we will discuss the influence of deviation from the pure gravitational potential later.

In such self-gravitating systems, the crossing time τ_c and the relaxation time τ_r are evaluated as $\tau_c \approx 1/\sqrt{G\rho} = 1/\sqrt{\rho}$ and $\tau_r \approx (0.1N/\ln N)\tau_c$, respectively, where ρ represents the density of the system [23]. In our units, the crossing and relaxation times are $\tau_c \approx 0.1$ and $\tau_r \approx 0.6$, respectively, assuming a uniform density profile, i.e., $\rho = mN/(4\pi R^3/3)$. The collapse time of the present system is approximately 600, since the collapse time in a system with $N=125-250$ particles and $r_0=0.005R$ is approximately $\sim 10^3 \tau_r$ [43].

III. INITIAL CONDITIONS

For an initial setup, we prepare a self-gravitating system at an approximate virial equilibrium state as follows:

(i) Step I: all the particles initially are distributed randomly in the spherical container based on a spherically symmetric uniform density profile. Moreover, all the particles are set to have a velocity of $|\mathbf{v}|$ but with a random direction. The velocities $\mathbf{v}$ are set to keep a total energy of 0.5, which is higher than the explosion energy $\varepsilon_{expl} \approx 0.267$. Thereafter, to keep the total momentum and the total angular momentum 0, the velocities of the particles are slightly modified taking into account the spherically symmetric uniform density profile.

(ii) Step II: the N-body simulation is carried out under a restriction of constant energy. That is, the reflecting wall is set to be the adiabatic wall. To obtain a quasiequilibrium state, the microcanonical ensemble simulation is continued over 10 units of time, i.e., for $t'=10$, where t' represents the time for the initial setup. We have confirmed that the system
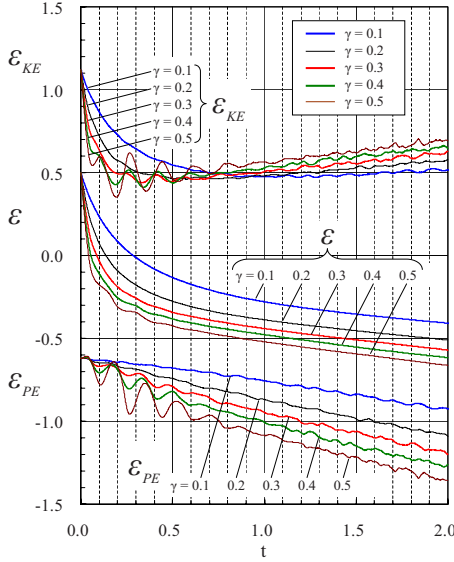
FIG. 1. (Color online) Time evolutions of the total energy ε, kinetic energy ε_{KE}, and potential energy ε_{PE}.

is in an approximate virial equilibrium state at $t' = 10$ using the virial ratio $\alpha(t)$ of the system,

$$\alpha(t) = \frac{2E_{KE} - 4\pi R^3 P_{wall}}{|E_{PE}|}, \tag{7}$$

where P_{wall} represents the pressure on the container wall [37,42]. Note that the virial ratio is 1 if the system is in the virial equilibrium state with pure gravitational potentials.

To check the above obtained system, we have examined density profiles. As a result, the density profile is not exactly uniform at $\varepsilon_0 = 0.5$, which is generally considered as the uniform state. However, we have confirmed that the system is in an approximate virial equilibrium state using the virial ratio. Therefore, in our simulations, we employ the above obtained system as the source for the initial setup. The initial energies are $\varepsilon_0 = 0.5000 \pm 0.0096$, $\varepsilon_{KE_0} = 1.1206 \pm 0.0109$, and $\varepsilon_{PE_0} = -0.6206 \pm 0.0076$, where the errors indicate the 68% confidence level in terms of the normal error distribution. We have confirmed that our main results do not greatly depend on the initial total energy, e.g., $\varepsilon_0 = 0.3$.

Using the initial setup, a simulation for the system with a nonadiabatic wall is carried out with various cooling rates γ. For $\gamma = 0.001$, 0.01, 0.1, and 0.2–0.5, the simulation time is $t = 100$, 18, 4, and 2, respectively. Accordingly, our simulation time should be shorter than the collapse time of the present system, ~ 600; that is, we examine an early relaxation process before the collapse. Only the above microcanonical ensemble simulation is carried out, as for $\gamma = 0$.

IV. RESULTS

A. Energies and temperature of the system

To examine the influence of the cooling rate, we first observe typical time evolutions of the energies for $\gamma = 0.1$, 0.2, 0.3, 0.4, and 0.5. As shown in Fig. 1, the total energy ε decreases rapidly with time t because of the nonadiabatic
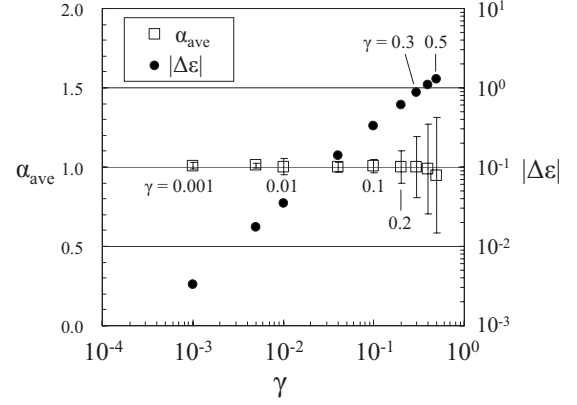

FIG. 2. Averaged virial ratio α_{ave} and initial energy loss $|\Delta\varepsilon|$ for various cooling rates γ. The virial ratio is averaged over $t \approx 0 - \tau_c$. The initial energy loss $|\Delta\varepsilon|$ is given by $|(d\varepsilon/dt)_{t \approx 0}| \times \tau_c$.

wall (hereafter we call the first stage the *rapid initial cooling stage*). Each curve gradually tends to a gentle incline after the rapid initial cooling stage, since both the velocity and the density near the wall reduce as the total energy decreases. We found that, the greater the cooling rate, the more rapid the decrease in the total energy.

Similarly, the time evolution of the kinetic energy ε_{KE} in Fig. 1 exhibits a decrease with time during the rapid initial cooling stage. However, the kinetic energy gradually increases after this stage, while the total energy decreases. In other words, the kinetic energy increases with decreasing total energy, i.e., $d\varepsilon/d\varepsilon_{KE}$ is negative. If the kinetic energy corresponds to the temperature of the system, then this indicates that an incidence of negative specific heat occurs.

As shown in Fig. 1, for $\gamma = 0.3$, 0.4, and 0.5, we find that the kinetic and potential energies oscillate considerably during the rapid initial cooling stage, after which the amplitude of the oscillations decays. The period of the oscillations is approximately ~ 0.2. Therefore, the period seems to be related to the crossing time, $\tau_c \approx 0.1$, which is proportional to the period of plasma oscillations in a medium with charge concentration [42]. (We have confirmed that the oscillation shown in Fig. 1 does not greatly depend on the average operation and the time step. However, the oscillation may disappear when the number of particles is large [44].) After the rapid decrease in the kinetic energy, the first minimum of the potential energy appears at time $t \approx 0.1$ corresponding to the crossing time τ_c. We expect that the extent of the decrease in energy is too large to maintain the virial equilibrium state and that the virial ratio significantly deviates from 1 during the rapid initial cooling stage.

To examine this, we observe the virial ratio with various cooling rates ($\gamma = 0.001 - 0.5$). The value of the virial ratio $\alpha(t)$ given by Eq. (7) is averaged over $t \approx 0 - 0.1$ to observe the averaged behavior of the rapid initial cooling stage. As shown in Fig. 2, the averaged virial ratio α_{ave} is approximately 1, although the value seems to decrease slightly at large values of γ. However, the error bars, i.e., the standard deviation of α_{ave}, start to increase at $\gamma = 0.2$ and then rapidly increase with γ. This means, for $\gamma \gtrsim 0.2$, the virial ratio oscillates considerably during this stage. In contrast, the initial energy loss $|\Delta\varepsilon|$ depends clearly on γ and the order of $|\Delta\varepsilon|$ is
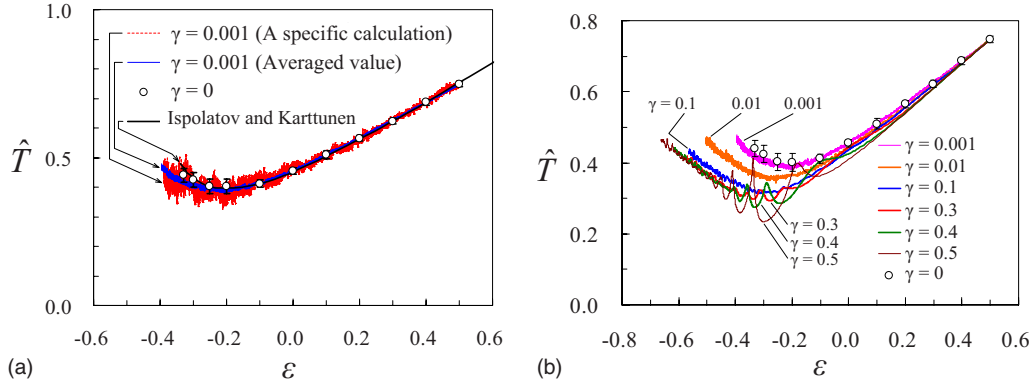
FIG. 3. (Color online) (a) Dependence of the temperature $\hat{T}$ on the total energy ε for the microcanonical ensemble ($\gamma=0$, the Ispolatov and Karttunen work [43]) and a nonequilibrium process ($\gamma=0.001$). (b) Dependence of the temperature $\hat{T}$ on the total energy ε for various cooling rates γ. For simplicity, typical results are plotted. Note that, as for $\gamma>0$, the simulation starts from an initial total energy of $\varepsilon_0=0.5$. The values for $\gamma=0$ are averaged over at least ten simulations and over $t'=9-10$.

1 for $\gamma=0.3$, 0.4, and 0.5. That is, the initial energy loss is too large to keep a quasiequilibrium state in the present system.

The system considered above is different from microcanonical ensembles, since the total energy is not fixed. Nevertheless, if the cooling rate is sufficiently small, the specific heat of the system or the relationship between energy and temperature may approach that for a microcanonical ensemble. Accordingly, we examine a system with a small cooling rate, $\gamma=0.001$, for comparison with a microcanonical ensemble.

To observe the properties of the microcanonical ensemble, two results are shown in Fig. 3(a). The first is our simulation result ($\gamma=0$), for which the total energy ε is varied from 0.5 to -0.33. The second is from the work of Ispolatov and Karttunen [43]; a high-energy branch terminating at the collapse energy $\varepsilon_{coll}\approx-0.339$ is plotted for the uniform state. Taking into account a comparison with their work, we calculate the temperature $\hat{T}$ from the kinetic energy using Eq. (4). As shown in Fig. 3(a), our microcanonical ensemble simulation ($\gamma=0$) agrees well with the Ispolatov and Karttunen work; that is, we can confirm that the kinetic energy corresponds to the temperature of the system at an approximate virial equilibrium state. For $-0.2\lesssim\varepsilon$, the temperature $\hat{T}$ increases with the total energy ε. Accordingly, the system behaves like an ideal gas with a positive specific heat, i.e., $d\varepsilon/d\hat{T}>0$. In contrast, for $\varepsilon\lesssim-0.2$, the temperature decreases with increasing total energy. In other words, the specific heat in this region is negative, i.e., $d\varepsilon/d\hat{T}<0$.

Now, we focus on the result for a system with a nonadiabatic wall, i.e., $\gamma=0.001$. The simulation starts from an initial total energy of $\varepsilon_0=0.5$, as shown in Fig. 3(a). For $-0.2\lesssim\varepsilon$, the total energy and the temperature decrease from the initial value because of the nonadiabatic wall. In this region, we find excellent agreement between $\gamma=0.001$ (a nonequilibrium process) and $\gamma=0$ (microcanonical ensemble). In contrast, for $\varepsilon\lesssim-0.2$, while a specific calculation oscillates considerably due to statistical fluctuations, we can observe a negative specific heat from the averaged value, since the temperature increases with decreasing ε. Moreover, as ex-

pected, the result for $\gamma=0.001$ agrees well with the microcanonical ensemble. Note that the temperature for $\gamma=0.001$ is slightly lower than that for $\gamma=0$. If the cooling rate is smaller than $\gamma=0.001$, the dependence of temperature on energy can further approach that of the microcanonical ensemble. However, when γ is too small, the system should undergo a collapse since the simulation time is longer than the collapse time. (If the simulation time is longer than the collapse time, our $\varepsilon-\hat{T}$ curve may be extended to a core-halo or low-energy branch terminating at the explosion energy ε_{expl}, where the low-energy (core-halo) branch is located above the high-energy branch for the uniform state [43]. However, through the present study, the simulations are carried out below $\hat{T}\sim0.5$ to examine the $\varepsilon-\hat{T}$ curve near the high-energy branch before the collapse. For simulating a system at lower-energy and higher-temperature states, smaller time steps and longer computational time are required to maintain the accuracy of the simulations. Accordingly, we would leave such a long-term simulation for the future research.)

Finally, we examine the influence of the cooling rate more closely by investigating the dependence of the temperature on the total energy for various cooling rates. As shown in Fig. 3(b), for $-0.2\lesssim\varepsilon$, the curve further deviates from the microcanonical ensemble ($\gamma=0$) with increasing cooling rate γ [45]. That is, the greater the cooling rate, the steeper the slope of the curve. This is because the system deviates from the virial equilibrium state, since the decrease in the kinetic energy is rapid due to the large cooling rate. For $\varepsilon\lesssim-0.2$, or rather $\varepsilon\lesssim\varepsilon_{coll}$, the temperature increases with decreasing total energy, excepting several large oscillations. Therefore, it is clearly demonstrated that a negative specific heat occurs in the system with various cooling rates assuming that the kinetic energy corresponds to the temperature of the system. (In fact, this assumption should be accepted, since all the systems are in an approximate virial equilibrium state except around the large oscillations and the rapid initial cooling stage.) In particular, it seems that each curve gradually shifts toward a common curve and that the extent of the negative specific heat or $d\varepsilon/d\hat{T}$ does not greatly depend on the cooling rate. For example, the saddle point or the bottom of the

curve seems to shift to $\varepsilon \approx \varepsilon_{coll}$. This is probably because the influence of the gravitational potential is extremely large for $\varepsilon \lesssim \varepsilon_{coll}$. The tendency toward a common curve, confirmed for our results even for $\gamma = 0.5 - 1.0$, remains an open question. (We have confirmed the tendency toward a certain common curve even for $r_0 = 0.050R$.) Therefore, we will investigate the tendency toward a common curve in the following.

Recently, Taruya and Sakagami [23–27] have clearly shown that an extremum state of Tsallis' generalized entropy, i.e., the *stellar polytrope*, has a consistent thermodynamic structure, which predicts thermodynamic instability because of a negative specific heat. Moreover, they found that a stellar polytropic distribution is expected to be quasiattractors of self-gravitating systems. In fact, we expect that a quasiequilibrium structure of the stellar polytrope should be related to our nonequilibrium process appearing in the self-gravitating system with nonadiabatic walls. In this context, we examine the present nonequilibrium process by comparing with the stellar polytrope.

We first give a brief review of the stellar polytrope according to the works of Taruya and Sakagami [26,27]. In their works, the polytropic relation can be given as

$$P(r) = K_n \{\rho(r)\}^{1+1/n}, \quad (8)$$

where K_n, $P(r)$, and $\rho(r)$ are the dimensional constant, the isotropic pressure, and density at radius r, respectively. The polytrope index n is given by

$$n = \frac{1}{1-q} + \frac{1}{2}, \quad (9)$$

where q is the Tsallis' entropic parameter. Let us consider a *quasiequilibrium* structure of the stellar polytropic system enclosed in a spherical container with *adiabatic* walls. Consequently, in our units, the total energy and temperature of the system are given by

$$\varepsilon = \frac{1}{n-5} \left\{ \frac{3}{2} \left(1 - \frac{n+1}{v_e} \right) + (n-2) \frac{u_e}{v_e} \right\}, \quad (10)$$

$$\hat{T} = \frac{n+1-2u_e-v_e}{(n-5)v_e}, \quad (11)$$

where u_e and v_e are homology invariants at the wall. The homology invariants are obtained from *Emden solutions* [46]. The details are summarized in Refs. [26,27].

The nonequilibrium process for various cooling rates and the stellar polytrope obtained from Eqs. (10) and (11) are shown in Fig. 4. In this figure, for the nonequilibrium process, we plot not only typical results shown in Fig. 3 but also the result for $\gamma = 0.8$. (For $\gamma = 0.8$, the simulation time is $t = 2$.) For the stellar polytrope, we plot trajectories of Emden solutions for polytrope indices of $n = 5$, 12, and ∞. The polytrope index of $n = \infty$ corresponds to isothermal spheres or microcanonical ensembles (For details, see the Appendix and Fig. 10.). Note that the softening parameter for the Plummer softened potential is $r_0 = 0.005R$ in our N-body simulations, while the pure gravitational potential is assumed for the stellar polytrope. Accordingly, we have to take into account the influence of the softening parameter.
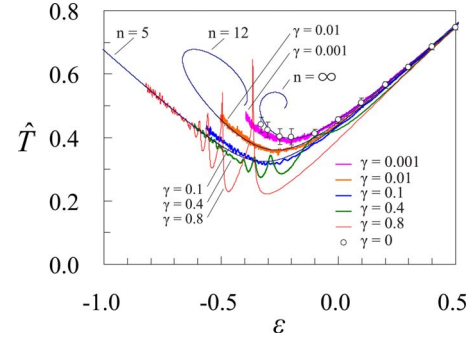

FIG. 4. (Color online) Dependence of the temperature $\hat{T}$ on the total energy ε for various cooling rates γ and polytrope indices n. Trajectories of Emden solutions with $n = 5$, 12, and ∞ are indicated for the stellar polytrope.

As shown in Fig. 4, our microcanonical ensemble simulations ($\gamma = 0$) are consistent with the isothermal sphere ($n = \infty$) except for a part of the spiral curve. (The difference between $\gamma = 0$ and $n = \infty$ indicates the influence of deviation from the pure gravitational potential.) Moreover, the $\varepsilon - \hat{T}$ curve for $\gamma = 0.01$ agrees well with the curve for the polytrope index of $n = 12$ except for a part of the spiral curve. Therefore, the $\varepsilon - \hat{T}$ curve for various cooling rates seems to correspond to the $\varepsilon - \hat{T}$ curve for various polytrope indices. In other words, the stellar polytrope should be consistent with a behavior of the nonequilibrium process appearing in the self-gravitating system with the nonadiabatic wall.

As described above, the $\varepsilon - \hat{T}$ curve varies from the microcanonical ensemble to a certain common curve with increasing cooling rates. Interestingly, the common curve appearing in the present nonequilibrium process agrees well with the $\varepsilon - \hat{T}$ curve for the polytrope index of $n = 5$ as shown in Fig. 4. (If the pure gravitational potential, i.e., $r_0 = 0$, is employed for our simulation, a common curve moves upward slightly. Accordingly, we expect that the common curve for $r_0 = 0$ should agree with the $\varepsilon - \hat{T}$ curve for $n \sim 5$ or rather $n > 5$.) As a matter of fact, the polytrope index of $n = 5$ indicates the appearance of gravothermal instability for the stellar polytrope within an adiabatic wall [26,27]. That is, for $n > 5$, the stellar polytrope within the adiabatic wall exhibits the gravothermal instability. Therefore, the stellar polytrope with $n \sim 5$ should be related to a quasiattractor of the present nonequilibrium process.

To observe an overview of density profiles, we select three conditions from Fig. 4 as follows: for $\gamma = 0.8$, 0.4, and 0.1, the temporal total energy is approximately $\varepsilon = -0.80$ (at $t = 1.83$), $\varepsilon = -0.6$ (at $t = 1.86$), and $\varepsilon = -0.4$ (at $t = 1.92$), respectively. In Fig. 5, the density profiles for the present nonequilibrium process are indicated as the symbols, i.e., $\bigcirc$, $\triangle$, and $\square$. Each real line represents the Emden solution with $n = 5$, which is fitted with the corresponding simulation result, using Eq. (A.7) in Ref. [26] or Eq. (3.22) in Ref. [27]. As shown in Fig. 5, each curve for the stellar polytrope with $n = 5$ can be well fitted with the simulation result. Of course, the stellar polytrope considered here is assumed to be quasiequilibrium structures of the system enclosed in a spherical
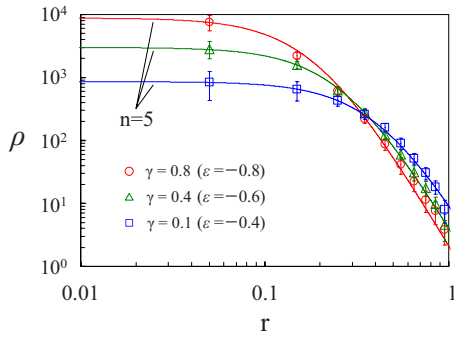
FIG. 5. (Color online) Density profiles for the nonequilibrium process and the stellar polytrope. The symbols represent the simulation results for the nonequilibrium process. The real lines represent the stellar polytrope with $n=5$. For the nonequilibrium process, the origin of r is set to be the center of gravity.

container with adiabatic walls. However, these results indicate that the behavior of the present nonequilibrium process should be consistent with the stellar polytrope.

B. Local properties of the system

In this subsection, we observe the local properties of the system simulated in Sec. IV A to examine the influence of nonadiabatic walls. For this purpose, we investigate a shell-averaged value. To calculate the shell-averaged value, we consider the following imaginary shells: in the spherical container of radius $R=1$, the container is divided into ten spherical shells in the radial direction r. The distance between the inner and outer shells is set to be $\Delta r=0.1$. Note that the origin of r is set to be the center of gravity in the present study, since the center of gravity moves slightly through the simulations. That is, for calculating a shell-averaged value,
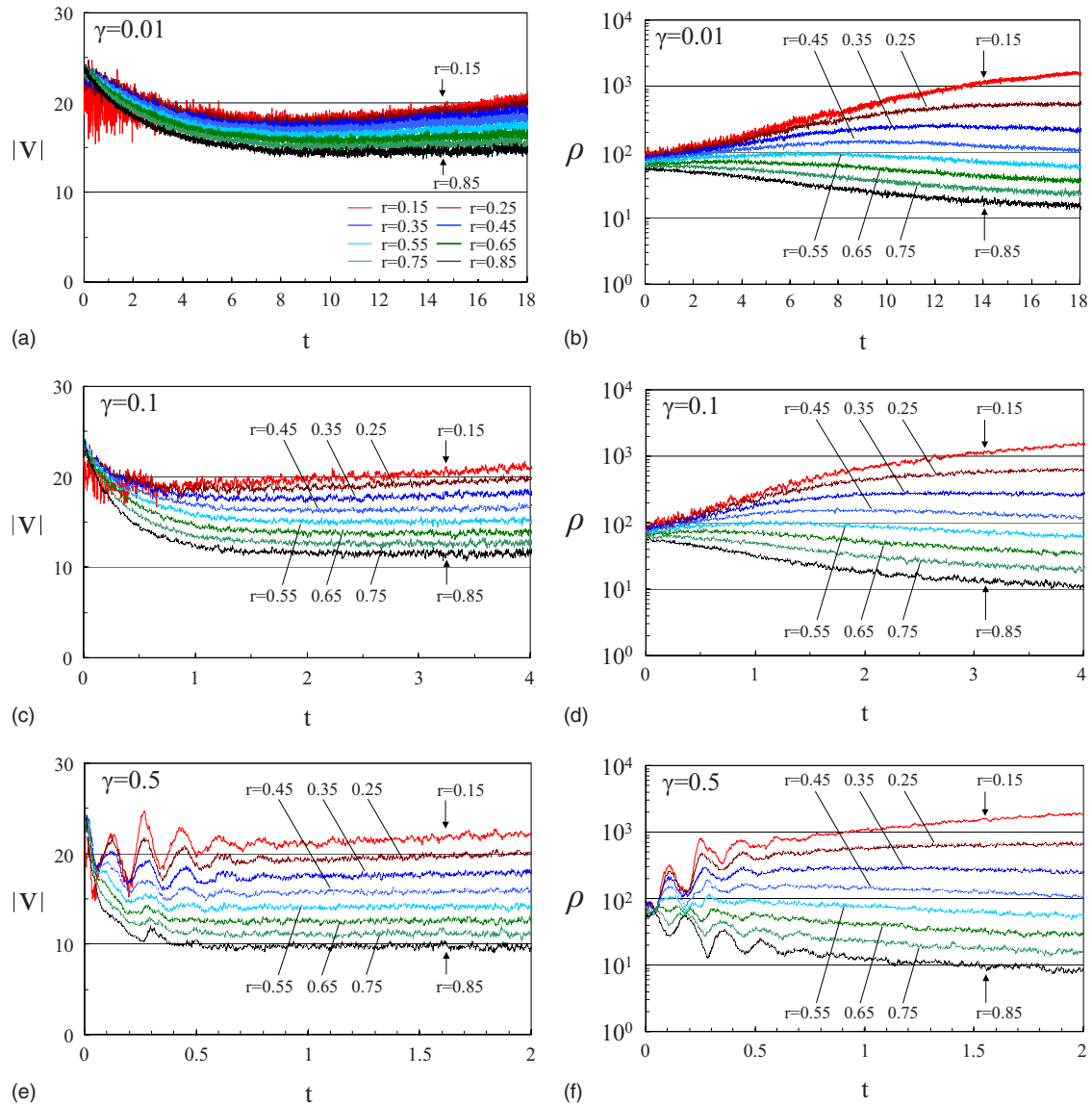

FIG. 6. (Color online) Time evolutions of the shell-averaged velocity (left) and density (right) for each shell. The cooling rate is set to be $\gamma=0.01$ (top), $\gamma=0.1$ (middle), and $\gamma=0.5$ (bottom), respectively. The results are averaged over 30 simulations with identically prepared initial setups. The r values, i.e., $r=0.15-0.85$, are the midpoint radius within the shell (see the text).
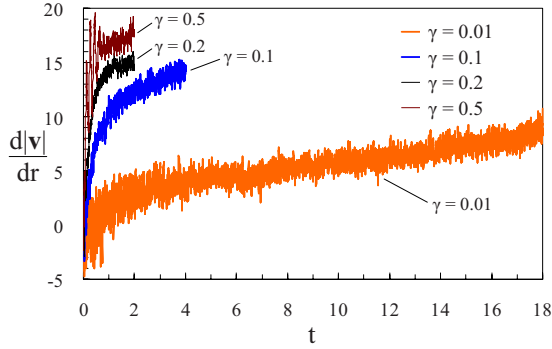
FIG. 7. (Color online) Time evolutions of the velocity gradient for various cooling rates γ. As a typical velocity gradient, $\frac{d|\mathbf{v}|}{dr}\big|_{0.75}^{0.25}$ is plotted.

FIG. 8. Velocity gradients for various cooling rates γ. The velocity gradients at time $t=2$ are indicated.

we consider the imaginary spherical shells which are fixed at the center of gravity. The value in the shell is averaged over 30 simulations. In the following, we discuss the shell-averaged value except for the innermost and outermost shells to observe an overview of the local properties [47].

We first examine time evolutions of a shell-averaged velocity and density for $\gamma=0.01$, 0.1, and 0.5 as shown in Fig. 6. The shell-averaged velocity considered here is the shell-averaged velocity speed. In this figure, for instance, the curve with "$r=0.85$" (or "$r=0.15$") represents a shell-averaged value between $r=0.8$ and $r=0.9$ (or between $r=0.1$ and $r=0.2$). As shown in Fig. 6(a) and 6(c), each shell-averaged velocity reduces with time during the rapid initial cooling stage. Thereafter, the velocity in an inner region, i.e., for $r \approx 0.15-0.25$, gradually increases. The shell-averaged density in the inner region increases with time as shown in Fig. 6(b) and 6(d). These indicate that an incidence of negative specific heat occurs. On the other hand, in an outer region, i.e., for $r \approx 0.65-0.85$, the shell-averaged velocity and density should reduce with time. Therefore, the behavior of the inner region is different from that of the outer region.

Now, we observe the influence of the nonadiabatic wall with various cooling rates. To this end, we focus on the outer shell near the wall, i.e., $r=0.85$. As shown in Fig. 6(a), 6(c), and 6(e), the decrease in the velocity for $r=0.85$ is the largest and the most rapid. The shell-averaged velocity for $\gamma=0.1$ [Fig. 6(c)] approaches a smaller value than that for $\gamma=0.01$
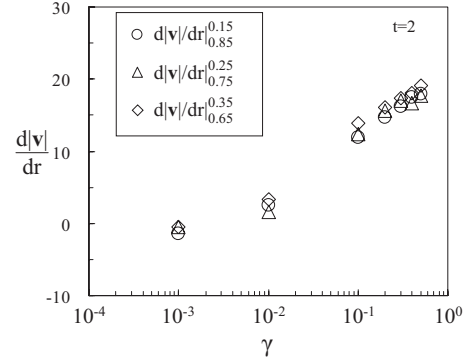
[Fig. 6(a)] because of the large cooling rate. Similarly, as for $r=0.85$, the shell-averaged density for $\gamma=0.1$ [Fig. 6(d)] seems to approach a smaller value than that for $\gamma=0.01$ [Fig. 6(b)]. However, for the large cooling rate of $\gamma=0.5$ [Fig. 6(e)], the velocity oscillates considerably during the rapid initial cooling stage, since the velocity reflected at the wall reduces rapidly. We find that the velocity in the inner region increases within the crossing time, $\tau_c \approx 0.1$. That is, the influence of the nonadiabatic wall propagates to the inner region within the crossing time. However, it should take at least the relaxation time, $\tau_r \approx 0.6$, for the amplitude of the oscillations to decay. The rapid change in the velocity significantly affects the density profile as shown in Fig. 6(f).

In later time shown in Fig. 6(a), 6(c), and 6(e), a spread of the shell-averaged velocity profiles or a velocity gradient between the inner and outer regions seems to increase as the cooling rate increases. To examine this, we observe local velocity gradients calculated from the shell-averaged velocity. In Fig. 7, we plot $\frac{d|\mathbf{v}|}{dr}\big|_{0.75}^{0.25}$ as one of the typical velocity gradients, where the velocity gradient is defined as

$$\frac{d|\mathbf{v}(r)|}{dr}\bigg|_{r_b}^{r_a} = \frac{|\mathbf{v}(r_a)| - |\mathbf{v}(r_b)|}{|r_a - r_b|}. \tag{12}$$

As shown in Fig. 7, the velocity gradients for $\gamma=0.1-0.5$ increase rapidly with time, while the velocity gradient for $\gamma=0.01$ gradually increases with time. In other words, the
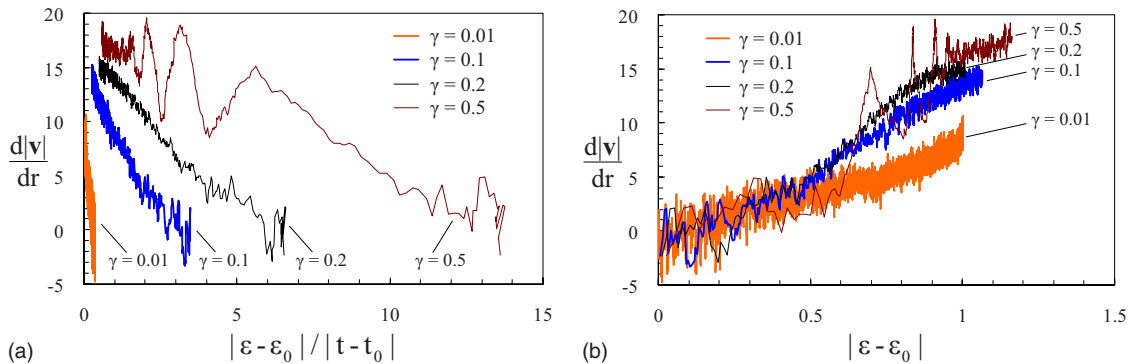

(a)

(b)

FIG. 9. (Color online) (a) Dependence of the velocity gradient on the rate of energy loss. (b) Dependence of the velocity gradient on the energy loss. In (a), each curve moves from right to left as time goes on. In (b), each curve starts from $|\varepsilon-\varepsilon_0|=0$, and $|\varepsilon-\varepsilon_0|>0.5$ corresponds to $\varepsilon(t)<0$. The velocity gradient $\frac{d|\mathbf{v}|}{dr}\big|_{0.75}^{0.25}$ shown in Fig. 7 is rearranged.

greater the cooling rate, the greater the velocity gradient in later time. To investigate the influence of the cooling rate more closely, we observe several velocity gradients at time $t=2$ as a function of the cooling rate. For this purpose, we examine three velocity gradients, i.e., $\frac{d|\mathbf{v}|}{dr}|_{0.85}^{0.15}$, $\frac{d|\mathbf{v}|}{dr}|_{0.75}^{0.25}$, and $\frac{d|\mathbf{v}|}{dr}|_{0.65}^{0.35}$. As shown in Fig. 8, the behavior of three velocity gradients is consistent with each other. As expected, the velocity gradients considered here increase with the cooling rate. That is, it is clearly shown that the cooling rate or the nonadiabatic wall affects the velocity gradient of the system.

In the above discussion, an energy loss or a rate of energy loss is different at each time. Accordingly, we rearrange Fig. 7 and show Fig. 9 as a function of the energy loss and the rate of energy loss. In Fig. 9, the energy loss and the rate of energy loss are given by $|\varepsilon(t)-\varepsilon_0|$ and $|\varepsilon(t)-\varepsilon_0|/|t-t_0|$, respectively. Here ε_0 and t_0 represent an initial total energy of 0.5 and an initial time of 0.

As shown in Fig. 9(a), the behavior of each curve depends on the cooling rate, since the rate of energy loss is different from each other even initially. (Note that each curve moves from right to left as time goes on.) For example, the rate of energy loss for $\gamma=0.01$ is smaller than the others because of the low cooling rate. On the other hand, as shown in Fig. 9(b), the velocity gradient should not greatly depend on the cooling rate, for $|\varepsilon-\varepsilon_0|<0.5$ corresponding to $\varepsilon(t)>0$. However, for $|\varepsilon-\varepsilon_0|>0.5$ or $\varepsilon(t)<0$, the velocity gradient depends on the cooling rate. In other words, for $\varepsilon(t)<0$ or in a gravity-dominated state, the velocity gradient for $\gamma=0.1-0.5$ increases more rapidly than that for $\gamma=0.01$; i.e., the greater the cooling rate, the greater the velocity gradient. This means that the cooling rate affects the velocity gradient especially in the gravity-dominated state.

V. CONCLUSIONS

To clarify the negative specific heat appearing in self-gravitating systems, we examined a system enclosed in a spherical container with adiabatic and nonadiabatic walls by means of N-body simulations. For nonequilibrium processes, a particle reflected at a nonadiabatic wall was cooled to mimic energy loss by reflecting walls. Through the present study, we have shown that a negative specific heat occurs not only in microcanonical ensembles but also in certain nonequilibrium processes with various cooling rates. We found that with increasing cooling rates, the dependence of the temperature on energy, i.e., the $\varepsilon-\hat{T}$ curve, varies from the microcanonical ensemble to a common curve. Interestingly, the common curve appearing in the nonequilibrium process agrees with an $\varepsilon-\hat{T}$ curve for stellar polytropes especially for the polytrope index of $n\sim 5$. Therefore, it seems that the stellar polytrope with $n\sim 5$ corresponds to a quasiattractor of the nonequilibrium process appearing in the self-gravitating system with the nonadiabatic wall. Moreover, the $\varepsilon-\hat{T}$ curve
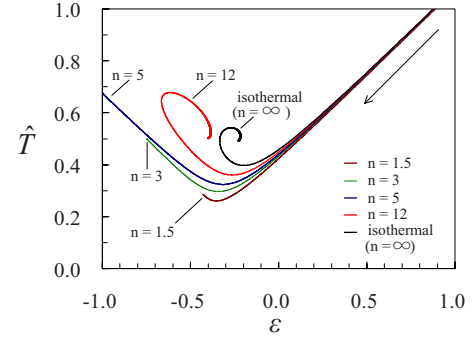

FIG. 10. (Color online) Trajectories of Emden solutions in $\varepsilon-\hat{T}$ plane for stellar polytropes. Each point along the trajectory represents the Emden solution evaluated at different values of radius r_e, where r_e represents the radius at the wall. All the trajectories start from $(\varepsilon,\hat{T})=(\infty,\infty)$ corresponding to the limit $r_e\to 0$. Accordingly, with increasing r_e, the trajectories move as indicated by the arrow. The trajectories for $n=5$, 12, and ∞ are plotted in Fig. 4 as well.

for various cooling rates is consistent with the $\varepsilon-\hat{T}$ curve for various polytrope indices. In other words, the present nonequilibrium process should be related to the stellar polytrope. In the nonequilibrium process, a rapid change in velocity at the nonadiabatic wall significantly affects the velocity and density profiles. The cooling rate affects the velocity gradient especially in a gravity-dominated state. That is, the greater the cooling rate, the greater the local velocity gradient in a low-energy region. The influence of the nonadiabatic wall has been revealed through the simulations. If the nonadiabatic wall considered here can be actualized, it will in principle be possible to control the specific heat of a long-range attractive interacting system.

APPENDIX: TRAJECTORIES OF EMDEN SOLUTIONS IN $\varepsilon-\hat{T}$ PLANE FOR STELLAR POLYTROPES

To observe the thermodynamic properties of stellar polytropes [26,27], we examine typical trajectories of Emden solutions in an $\varepsilon-\hat{T}$ plane as shown in Fig. 10. The polytrope index of $n=\infty$ corresponds to isothermal spheres and their characteristics have been investigated in detail [10]. As shown in Fig. 10, for larger energies, the system behaves like an ideal gas with a positive specific heat. In contrast, for smaller energies, the specific heat should be negative, i.e., $d\varepsilon/d\hat{T}<0$. Now, we focus on the influence of the polytrope index n. As examined by Taruya and Sakagami, the trajectories for $n>5$ gradually change their direction and finally spiral around a fixed point, while the trajectories for $n<5$ terminate suddenly because of the finite radius [26]. In fact, it is shown that, for $n>5$, the stellar polytrope within an adiabatic wall exhibits the gravothermal instability [26,27].

[1] V. A. Antonov, in *Dynamics of Globular Clusters*, IAU Symposium Vol. 113, edited by J. Goodman and P. Hut (Reidel, Dordrecht, 1985); Vestn. Leningr. Univ., Fiz., Khim. **7**, 135 (1962).

[2] D. Lynden-Bell and R. Wood, Mon. Not. R. Astron. Soc. **138**, 495 (1968).

[3] S. W. Hawking, Nature (London) **248**, 30 (1974).

[4] J. D. Bekenstein, Phys. Rev. D **9**, 3292 (1974).

[5] J. L. Lebowitz and E. H. Lieb, Phys. Rev. Lett. **22**, 631 (1969).

[6] W. Thirring, Z. Phys. **235**, 339 (1970).

[7] J. Binney and S. Tremaine, *Galactic Dynamics* (Princeton University Press, Princeton, 1987).

[8] C. Tsallis, J. Stat. Phys. **52**, 479 (1988).

[9] M. K. H. Kiessling, J. Stat. Phys. **55**, 203 (1989).

[10] T. Padmanabhan, Phys. Rep. **188**, 285 (1990).

[11] H. A. Posch, H. Narnhofer, and W. Thirring, Phys. Rev. A **42**, 1880 (1990).

[12] A. Plastino and A. R. Plastino, Phys. Lett. A **174**, 384 (1993).

[13] D. Lynden-Bell, Physica (Amsterdam) **263A**, 293 (1999).

[14] S. Abe, Phys. Lett. A **263**, 424 (1999).

[15] V. P. Youngkins and B. N. Miller, Phys. Rev. E **62**, 4583 (2000).

[16] E. Follana and V. Laliena, Phys. Rev. E **61**, 6270 (2000).

[17] J. Katz and I. Okamoto, Mon. Not. R. Astron. Soc. **317**, 163 (2000).

[18] I. Ispolatov and E. G. D. Cohen, Phys. Rev. Lett. **87**, 210601 (2001).

[19] I. Ispolatov and E. G. D. Cohen, Phys. Rev. E **64**, 056103 (2001).

[20] D. Fanelli, M. Merafina, and S. Ruffo, Phys. Rev. E **63**, 066614 (2001).

[21] P. H. Chavanis and I. Ispolatov, Phys. Rev. E **66**, 036109 (2002).

[22] R. Silva and J. S. Alcaniz, Phys. Lett. A **313**, 393 (2003).

[23] A. Taruya and M. Sakagami, Phys. Rev. Lett. **90**, 181101 (2003).

[24] A. Taruya and M. Sakagami, Mon. Not. R. Astron. Soc. **364**, 990 (2005).

[25] A. Taruya and M. Sakagami, Physica (Amsterdam) **307A**, 185 (2002); **318A**, 387 (2003).

[26] A. Taruya and M. Sakagami, Physica (Amsterdam) **322A**, 285 (2003).

[27] M. Sakagami and A. Taruya, Contin. Mech. Thermodyn. **16**, 279 (2004).

[28] A. Nakamichi and M. Morikawa, Physica (Amsterdam) **341A**, 215 (2004).

[29] P. H. Chavanis, Astron. Astrophys. **432**, 117 (2005).

[30] D. H. E. Gross, Physica (Amsterdam) **365A**, 138 (2006).

[31] W. Thirring, H. Narnhofer, and H. A. Posch, Phys. Rev. Lett. **91**, 130601 (2003).

[32] H. A. Posch and W. Thirring, Phys. Rev. Lett. **95**, 251101 (2005).

[33] H. A. Posch and W. Thirring, Phys. Rev. E **74**, 051103 (2006).

[34] M. D'Agostino *et al.*, Phys. Lett. B **473**, 219 (2000).

[35] M. Schmidt, R. Kusche, T. Hippler, J. Donges, W. Kronmuller, B. von Issendorff, and H. Haberland, Phys. Rev. Lett. **86**, 1191 (2001).

[36] N. Komatsu, T. Kiwata, and S. Kimura, Physica (Amsterdam) **387A**, 2267 (2008); **388A**, 1344 (2009).

[37] N. Komatsu, T. Kiwata, and S. Kimura, Physica (Amsterdam) **388A**, 639 (2009).

[38] N. Komatsu, S. Kimura, and T. Kiwata, Abstracts of Symposium Yukawa International Seminars (YKIS 2009), Kyoto, Japan (2009) (http://www2.yukawa.kyoto-u.ac.jp/~ykis2009/sympo_abstracts/komatsu.pdf); Abstracts of Mathematical Aspects of Generalized Entropies and Their Applications (Kyoto RIMS Workshop), pp. 9, Kyoto, Japan (2009) (to be published).

[39] If we examine energy loss by radiation in stars, a simple method such as reduction of all the velocities should be more suitable to mimic the energy loss. However, we employ the nonadiabatic wall to mimic energy loss by reflecting walls for certain nonequilibrium processes. This is because we examine the influence of the nonadiabatic wall on dynamical evolutions of the system especially on thermodynamic properties such as the incidence of negative specific heat.

[40] To mimic an inelastic wall and to decrease a variation in total angular momentum, a method which reduces only the radial component of the reflected velocity would be better than the present method. However, we employ the present method, since the present method can sufficiently mimic energy loss by nonadiabatic walls.

[41] E. V. Votyakov, H. I. Hidmi, A. De Martino, and D. H. E. Gross, Phys. Rev. Lett. **89**, 031101 (2002).

[42] I. Ispolatov and M. Karttunen, Phys. Rev. E **68**, 036117 (2003).

[43] I. Ispolatov and M. Karttunen, Phys. Rev. E **70**, 026102 (2004).

[44] T. E. C. Merrall and R. N. Henriksen, Astrophys. J. **595**, 43 (2003).

[45] Although this result should be predictable qualitatively, the influence of the nonadiabatic wall is clearly demonstrated quantitatively in the present study.

[46] S. Chandrasekhar, *Introduction to the Study of Stellar Structure* (Dover, New York, 1939).

[47] If a particle does not exist in the innermost shell, the value in the innermost shell is 0. In fact, the smallest volume of the innermost shell should cause a high incidence of a 0 *value*, when the density is low. Consequently, the shell-averaged value for the innermost shell includes large fluctuations or errors through our average operation. Similar things should arise in the outermost shell. Therefore, we do not discuss the shell-averaged values in the innermost and outermost shells, since these results are misleading.